Unifying Scaling Relations and Multiple Reaction Mechanisms for Screening Transition Metal-Doped Co_3O_4 for Oxygen Evolution Reaction

Kapil Dhaka,[1] Hatem M.A. Amin,[2] Davide Beschi,[3] Dana Schellenburg,[3] Benjamin Mockenhaupt,[3] Stephan Barcikowski,[3,4] Stephan Schulz,[2,4] Kai S. Exner[1,4,5,*]

[1] *University of Duisburg-Essen, Faculty of Chemistry, Theoretical Catalysis and Electrochemistry, Universitätsstraße 5, 45141 Essen, Germany*

[2] *University of Duisburg-Essen, Faculty of Chemistry, Institute of Inorganic Chemistry, Universitätsstraße 5, 45141 Essen, Germany*

[3] *University of Duisburg-Essen, Faculty of Chemistry, Technical Chemistry I, Universitätsstraße 5, 45141 Essen, Germany*

[4] *Center for Nanointegration (CENIDE) Duisburg-Essen, 47057 Duisburg, Germany*

[5] *Cluster of Excellence RESOLV, 44801 Bochum, Germany*

* Corresponding author: kai.exner@uni-due.de ORCID: 0000-0003-2934-6075 (KSE)

Abstract

Accelerating the discovery of oxygen-evolution reaction (OER) catalysts requires high-throughput screening strategies combining descriptor-based frameworks with dedicated mechanistic analyses. In this study, we present a unified methodology using the example of doped Co_3O_4 in the OER by developing a mechanistically resolved, potential-dependent volcano approach that accounts for the uncertainty of adsorption free energies when analyzing activity trends. We evaluate the influence of different dopants (Cr, Mn, Fe, Ni, Cu, and V) on the OER activity by selectively substituting octahedral Co sites on the (001) facet of Co_3O_4 using density functional theory calculations (DFT). We identify Cr, Fe, Ni, and V as promising dopants as they exhibit increased OER activity compared to undoped Co_3O_4, while Cr shows the strongest promoting effect among all dopants considered in this study. We compare our theoretical predictions with two different series of synthesized Co_3O_4 nanoparticle catalysts and find good agreement regarding the qualitative trends of OER activity. To validate the strong promoting effect of Cr, we synthesize surface-enriched, Cr-doped Co_3O_4 nanoparticles, which confirms the theoretical prediction of increased OER activity. The theoretical model developed in this work is a transferable framework that can be equally applied to other materials and electrocatalytic processes for quantifying dopant effects by considering uncertainty and promoting effects when analyzing activity trends.

Keywords

oxygen evolution reaction; Co_3O_4; descriptor approach; reaction mechanism; density functional theory; nanoparticle catalyst

1 Introduction

Rapid identification of efficient electrocatalysts for oxygen evolution reaction (OER) — 2 H_2O → O_2 + 4 H^+ + 4 e^-, U^0_{OER} = 1.23 V vs. RHE (reversible hydrogen electrode) — calls for screening strategies that traverse large compositional spaces while preserving mechanistic fidelity.[1] Descriptor-based frameworks and volcano plots have emerged as powerful tools for high-throughput screening of OER catalysts using adsorption free energies.[2,3] It is a unifying consensus that the adsorption free energies of the key OER intermediates, *OH, *O, and *OOH, are intrinsically coupled.[4,5] These correlations manifest as linear scaling relationships, typically expressed as ΔG_{*O} vs ΔG_{*OH} and ΔG_{*OOH} vs ΔG_{*OH}, which reduce dimensionality but also impose intrinsic constraints on catalyst optimization.[6] As a result, activity trends are often summarized by relying on the ΔG_{*OOH} vs ΔG_{*OH} relation in the form of a volcano plot that projects materials' performance onto a single binding-energy axis.[5,7,8] This approach has gained cult status in the community based on the ease of testing catalytic materials *in silico* using thermodynamic considerations.[9]

Most work in the OER literature use the mononuclear pathway,[10] which consists of the sequential formation of the *OH, *O, and *OOH adsorbates, to describe the proton-coupled electron transfer steps culminating into the formation of gaseous oxygen at a single active site[5,10]. Real oxide surfaces, especially doped ones, can access dual-site and multi-site routes.[11,12] Dopants may act as the active centers or as promoters that modulate the electrocatalytic activity of active sites through electronic and geometric effects.[13] Such cooperative behavior enables bifunctional, binuclear, Walden-type, and oxide-mediated mechanisms, which can compete with or surpass the mononuclear description depending on the local environment.[14–16] However, screening frameworks that allow for the inclusion of mechanistic diversity while relying on effective descriptors using the concept of adsorption free energies are lacking in the literature.

Substitutional doping is a particularly effective lever to enhance the electrocatalytic activity: introducing 3d transition metals (TM) into a robust oxide host can tune electronic structure, modulate metal-oxygen covalency, reshape adsorption energetics, and stabilize reactive surface states. Several works in the literature have addressed doping effects for spinel cobalt oxide (Co_3O_4) for OER,[17–30] although detailed atomic-level insights explaining the targeted doping are lacking. This requires theoretical considerations analyzed with volcano-based approaches that go beyond the mononuclear pathway and a single active site to carefully scan

the vast parameter space of doped Co_3O_4 structures accessible to OER. On the other hand, electrocatalysts identified based on computational high-throughput screening often cannot be directly compared with experimentally synthesized catalysts due to the obvious length gap between atomic-scale models and nanoscale catalytic materials.

In the present work, we close the outlined knowledge gaps by introducing a universal methodology for TM-doped Co_3O_4 (dopants: Cr, Mn, Fe, Ni, Cu, V) to solve the impact of dopants on OER activity by analyzing promoting effects. In addition to a variety of different mechanistic descriptions, the scaling relationship ΔG_{*O} vs ΔG_{*OH}, a potential-dependent activity assessment using the $G_{max}(U)$ descriptor,[31,32] and multiple active site configurations are considered in the analysis of adsorption free energies for OER. Our theoretical framework is then coupled with different series of doped Co_3O_4 catalysts, which are experimentally tested for OER activity. While our calculations suggest that Cr as a dopant at the Co_3O_4 surface has the main promoting effect for OER, we validate our theoretical prediction by the synthesis and experimental characterization of a surface-enriched, Cr-doped Co_3O_4 nanocube using linear sweep voltammetry. [33–37]

2 Theoretical Model

All calculations were carried out within the framework of spin-polarized density functional theory (DFT) using the projector-augmented-wave formalism and the PBE exchange-correlation functional. On-site Coulomb interactions were treated with PBE+U for Co and the 3d transition metal dopants, with element-specific U values listed in the supporting information (SI). All further computational details are provided in section S1 of the SI.

2.1 Surface Models and Doping Schemes

The spinel structure of Co_3O_4 was adopted with a 2×2 (001) termination-B slab exposing four surface octahedral Co_{oct} cations (cf. **Figure S1**). Under OER conditions, the undercoordinated Co_{oct} surface sites are fully capped by *OH adsorbates, as evident from the construction of *ab initio* Pourbaix diagrams in previous works.[16,18,38] Therefore, we select the 2×2 Co_3O_4(001)-4*OH configuration (cf. **Figure 1a**) as a starting point for the investigation of dopant effects in the OER. Note that the use of Co_{oct} surface sites as the active site for OER is consistent with experimental and theoretical studies on this topic,[39–42] although it should be emphasized that neighboring Co_{oct} sites can serve as auxiliary sites (cf. **Figure 1a**) during the elementary steps

by acting as Brønsted acid or base.[38] By considering neighboring sites, we extend conventional models based on a single active site to an ensemble of different configurations for investigating the elementary steps for OER.

Substitutional doping is introduced by replacing Co_{oct} surface sites with a 3d transition metal (TM), namely V, Cr, Mn, Fe, Ni, or Cu (cf. **Figure 1b**). Doping is restricted to the outer octahedral layer that hosts OER intermediates; subsurface tetrahedral cations remain Co. The surface contains four exposed Co sites per cell, and we replace either one or two of them, which corresponds to a surface dopant fraction of 25% (1/4) or 50% (2/4), respectively. Across the entire slab, there are 28 Co atoms in total, so that the total dopant concentration is 3.6% (1/28) or 7.1% (2/28), which is on the order of magnitude of experimental studies on doped Co_3O_4.[27,28,43–47] All doped slabs are fully relaxed while retaining the same 4*OH arrangement to isolate the effect of cation substitution from changes in surface coverage.

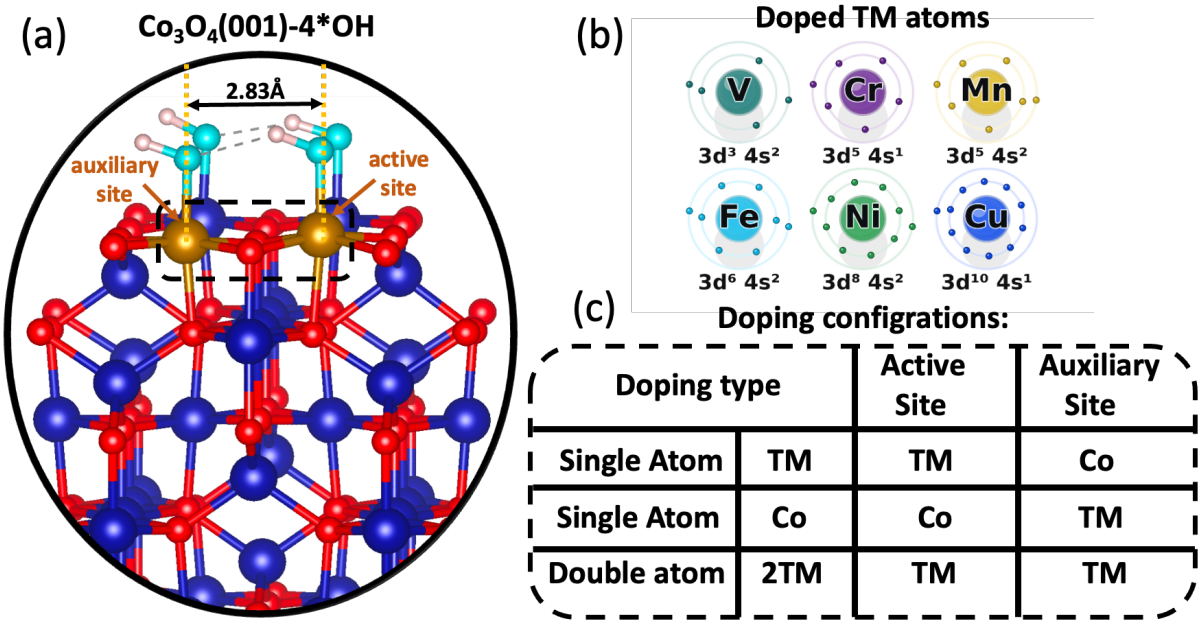

Figure 1. Schematic illustration of transition-metal (TM) doping for the thermodynamically stable Co_3O_4 (001)-4*OH surface. (a) Representative surface model highlighting the Co_3O_4(001) termination, with selected TM dopants (yellow) incorporated into surface Co sites. The structural motif shows the local environment of dopants and the TM-TM spacing (≅2.83 Å) relevant for catalytic activity. The auxiliary and active sites correspond to octahedrally coordinated cobalt sites (Co_{oct}). (b) Electronic configurations of the considered TM 3d dopants (V, Cr, Mn, Fe, Ni, Cu), depicted as atomic orbitals with valence electron distributions ($3d^n$,$4s^m$). (c) Dopant configurations summarized as single-atom doping (TM and Co are located at either the active or auxiliary sites) and double-atom doping (2TM refers to TM at the active site and auxiliary site both).

Three configurations are considered to separate intrinsic activity at the binding site from promotional effects of a neighbor (cf. **Figure 1c**):

- Active site TM, Auxiliary site Co (label "**TM**"): the active site is replaced by a dopant (cf. **Figure 1b**), and the auxiliary site remains Co.
- Active site Co, Auxiliary site TM (label "**Co**"): the active site remains Co, and the auxiliary site is replaced by a dopant.
- Active site TM, Auxiliary site TM (label "**2TM**"): both sites are replaced by the same dopant.

2.2 Computational workflow and analysis framework

Although the catalytic activity of electrocatalytic processes is determined by the kinetics (transition states) in the free-energy diagram along the reaction coordinate, there is consensus in the theoretical electrocatalysis community to rely on the determination of Gibbs free-energy changes (ΔG) for the elementary reaction steps of OER.[4,5,10] The main reason for this approach is that the calculation of transition states for proton-coupled electron transfer steps is computationally intensive and associated with significant errors,[48,49] making this strategy unsuitable for heuristic materials screening.[50] To this end, we apply the computational hydrogen electrode (CHE) approach[51] to determine potential-dependent $\Delta G(U)$ values for seven different OER mechanisms, which are summarized in section S2 of the SI. Further computational details on the determination of ΔG values by incorporating zero-point and entropy corrections for adsorbates and gas molecules, implicit solvation,[52] and the application of gas-phase error corrections[53,54] to overcome the DFT bias leading to incorrect prediction of reaction energies are given in section S1 of the SI. The potential-dependent $\Delta G(U)$ values for the different OER pathways are used to determine the electrocatalytic activity using the $G_{max}(U)$ descriptor,[31,32] which links thermodynamics to kinetics through a free-energy span model using the Brønsted-Evans-Polanyi relationship.[55] For a given reaction mechanism, the descriptor $G_{max}(U)$ is defined as:

$$G_{max}(U) = max_{1\leq p<q\leq N+1}\left[G_q(U) - G_p(U)\right] = max_{1\leq p<q\leq N+1} \sum_{k=p}^{q-1} \Delta G_k(U) \qquad (1)$$

In equation (1), N corresponds to the number of elementary steps (states indexed as 1, …, N+1); p and q are indices of two intermediate states (with the respective Gibbs free energy, G), which need to adhere to the condition $p < q$; k is a running index that ensures that all free-energy spans between the intermediate states are systematically evaluated. Typically, $N = 4$ for the four proton-coupled electron transfer steps in OER (thus, $p, q \in \{1, \ldots, 5\}$). In case certain mechanistic pathways include a chemical step in the description (cf. section S2 of the SI), then $N = 5$ and $p, q \in \{1, \ldots, 6\}$.

Based on the $G_{max}(U)$ values for the different mechanistic pathways, we can extract the energetically preferred description by referring to the lowest values; this descriptor is shown on the y axis of a volcano plot. In addition, the free-energy change between the *O and *OH intermediates is used as a descriptor on the x axis of a volcano plot based on previous work on the topic, although these works omitted the potential dependence of the OER volcano curve,[1,8,56–58] which is considered here. The trend line in the volcano plot is determined by a dedicated evaluation of the scaling relationships ΔG_{*O} vs ΔG_{*OH} and ΔG_{*OOH} vs ΔG_{*OH}, as further described in section S4 of the SI.

3 Results & Discussion

3.1 OER Mechanisms for Doped Co_3O_4(001) Systems

We investigate seven OER pathways on the pristine and TM-doped Co_3O_4(001)-4*OH surface using the active-site motifs in **Figure 1**. Free-energy diagrams at U = 1.37 V vs RHE are provided in section S3 of the SI (cf. **Figures S3–S8**). We choose U = 1.37 V vs RHE (η_{OER} = 0.14 V) as the target electrode potential for the energetic analysis to keep the free-energy spans (cf. equation (1)) meaningful and to exclude cases where $G_{max}(U)$ is negative. **Figure 2a** compiles these results by extracting for each composition and site motif the smallest $G_{max}(U)$ value among the seven OER pathways at U = 1.23 V and 1.37 V vs RHE. On the other hand, **Figure 2b** shows how the dopant placement (cf. **Figure 1c**) controls the electrocatalytic activity at U = 1.37 V vs RHE.

Across compositions, Walden-type mechanisms[50] often reveal the smallest value of the $G_{max}(U)$ descriptor, although they are not captured by the traditional screening framework, which relies on the energetics of the mononuclear description. The mononuclear mechanism could serve as a proxy for direction substitution of the active site (TM), consistent with direct tuning of the metal–adsorbate bond strength, although this mechanistic pathway is often not preferred for auxiliary site doping (Co) or the case of dual doping (2TM). Several systems achieve equal or lower spans when the dopant is placed at the neighboring auxiliary site (Co), suggesting a promoting effect through local hydrogen bond rearrangements and efficient proton removal during the proton-coupled electron transfer steps via bifunctional mechanisms. The dual-dopant case (2TM) does often not result in an enhanced catalytic activity; in some compositions, it matches the best single-site configuration, while in others, it deteriorates the

thermodynamic free-energy changes. This finding suggests that short-range TM–TM coupling can overstabilize certain intermediates. Raising the potential from 1.23 V to 1.37 V vs RHE generally lowers G_{max} but leaves the qualitative ranking largely unchanged, with oxide and binuclear pathways remaining comparatively less favorable on the doped Co_3O_4(001)-4*OH surface.

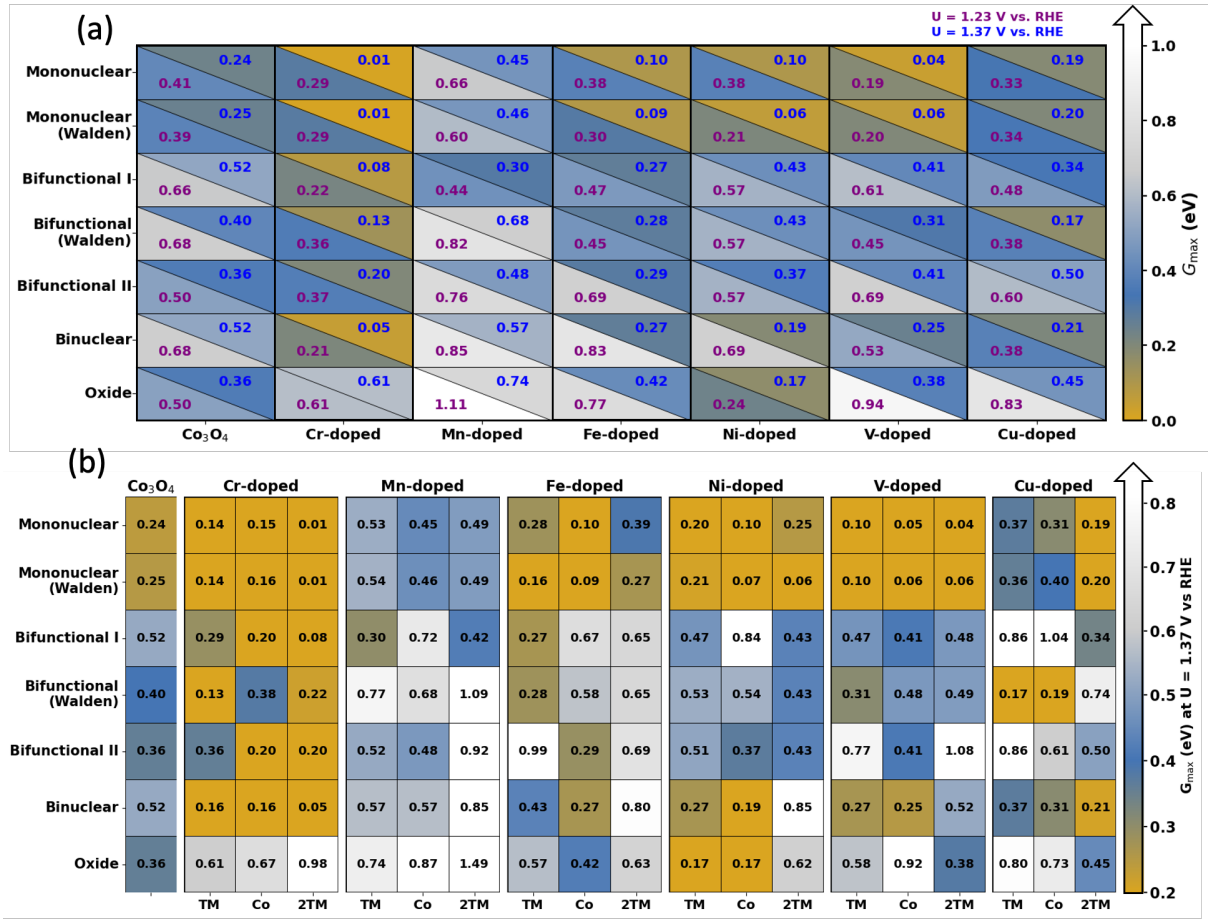

Figure 2. (a) Heatmap of $G_{max}(U)$ for Co_3O_4(001) and TM-doped variants (cf. **Figure 1**) across seven mechanisms. Rows list mechanisms; columns list catalyst systems. Each cell reports the lowest $G_{max}(U)$ among the different dopant configurations (TM/Co/2TM); purple and blue numbers correspond to U = 1.23 V and 1.37 V vs RHE, respectively. The color bar indicates $G_{max}(U)$ in eV. (b) Heatmap of $G_{max}(U)$ at U = 1.37 V vs RHE by differentiating between the different dopant configurations (TM/Co/2TM) in dependence on the mechanistic pathway. Note that a lower $G_{max}(U)$ value corresponds to higher OER activity.

In summary, the observed trends point to a simple design rule based on **Figure 2**: optimal performance is most often achieved by a single, judiciously placed dopant that either directly tunes the binding site or promotes it from the nearest neighbor, while the use of dual-dopant motifs (2TM) is generally not a great advantage given the present hydroxyl coverage of Co_3O_4 during OER.

Knowledge of the electrocatalytic activity based on the $G_{\max}(U)$ descriptor allows us to compare the effect of each dopant on the OER performance. While we provide a detailed analysis in section S3 of the SI (cf. **Figure S9**), we summarize here that Cr, Fe, Ni, V, and Cu as dopants enhance OER activity, while Mn-doped Co_3O_4 leads to a decrease in OER activity. A comparison of this result with experimental works on the topic is provided in sections 3.4 – 3.6.

3.2 Promoting Effect of Dopants on OER Activity

Typically, dopants are added to a material in low concentrations (less than 10%) to improve its catalytic properties. Considering that the majority of active sites retain the chemical nature of the original material, dopants can have two types of influence on catalytic activity: on the one hand, the dopants change the electronic structure of the active center due to their proximity, which is consistent with the case of auxiliary site doping (Co; cf. **Figure 1c**). On the other hand, the dopants can serve as an active center and form a minority species of active sites with a significantly higher electrocatalytic activity compared to the main active site. This scenario relates to the case of active site doping (TM; cf. **Figure 1c**). With increasing dopant concentration, the dopants can occupy both the active site and auxiliary site (2TM; cf. **Figure 1c**), which could further promote the activity of the electrocatalyst.

Based on the activity analysis in **Figure 2**, we evaluate the impact of the promoting effects of the selected dopants on the OER activity of $Co_3O_4(001)$. This is achieved by quantifying $\Delta G_{\max}(U)$, which is a measure of the change in electrocatalytic activity upon TM doping. This descriptor is defined as:

$$\Delta G_{max}^{\mathrm{A}\rightarrow\mathrm{B}}(U) = G_{\max}^{\mathrm{B}}(U) - G_{\max}^{\mathrm{A}}(U) \qquad (2)$$

In equation (2), the different states A and B of the $G_{\max}(U)$ descriptor refer to undoped-Co_3O_4, Co, TM, or 2TM (cf. **Figure 1c**). We inspect the transitions of undoped-Co_3O_4→Co, undoped-Co_3O_4→TM, Co→TM, and TM→2TM and quantify the corresponding change in electrocatalytic activity. Note that for each state, we use the $G_{\max}^{\mathrm{X}}(U)$ value, which is the minimum over all reaction mechanisms for the $Co_3O_4(001)$–4*OH model evaluated at $U = 1.37$ V vs RHE (cf. **Figure 2**). A negative $\Delta G_{max}^{\mathrm{A}\rightarrow\mathrm{B}}(U)$ transition indicates an improvement of the OER activity in the transition from A to B, which is related to a promoting effect of the dopant.

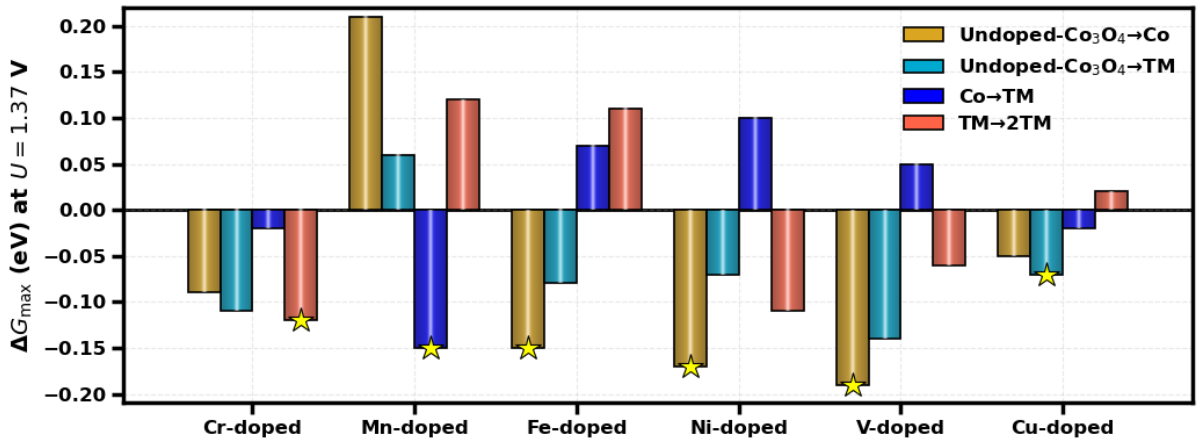

Figure 3. Change in the limiting free-energy span ($\Delta G_{max}(U)$, cf. equation (2)) at $U = 1.37$ V vs RHE for undoped and different TM-doped Co_3O_4 systems (cf. **Figure 1c**). Bars represent the effect of different doping configurations: Undoped-Co_3O_4→Co (gold), Undoped-Co_3O_4→TM (turquoise), Co→TM (blue) and TM→2TM (orange). Negative values correspond to a reduction in $G_{max}(U)$, which indicates a promoting effect of the respective dopant. Stars highlight the most favorable site configurations for each dopant.

Figure 3 illustrates that for Fe, Ni, and V doping, the undoped-Co_3O_4→Co transition is negative and corresponds to the minimum value of $\Delta G_{max}(U)$, indicating that these dopants are mainly suited as auxiliary promoters adjacent to a Co active site. These dopants also increase the OER activity when serving as the active site ($\Delta G_{max}(U) < 0$ for undoped-Co_3O_4→TM), although the effect is less pronounced compared to the case of the auxiliary site, assisted by a positive Co→TM transition. Increasing the local dopant concentration by inspecting the TM→2TM transition has little effect for both Ni and V, while it is expected to have a detrimental effect on Fe doping due to a positive $\Delta G_{max}(U)$ value. Therefore, we conclude that Fe, Ni, and V should be added mainly in small concentrations to the Co_3O_4 catalyst to activate active octahedral Co sites through electronic effects.

Mn doping is not preferential for Co_3O_4 in the OER, considering that the undoped-Co_3O_4→Co and undoped-Co_3O_4→TM transitions are positive. We note that the activity of Mn-doped Co_3O_4 increases if Mn switches from the auxiliary to the active site ($\Delta G_{max}(U) < 0$ for Co→TM), although we emphasize that the resulting electrocatalytic activity is still lower than that of undoped Co_3O_4 (cf. **Figure S9** in section S3 of the SI).

Cu doping has a small effect on the OER activity of Co_3O_4, considering that the $\Delta G_{max}(U)$ values for the undoped-Co_3O_4→Co and undoped-Co_3O_4→TM transitions are close to zero. Despite this, the Cu-doped Co_3O_4 is the only catalyst where the dopant as the active site corresponds to the preferential configuration for improved OER activity. Considering that at typical dopant concentrations of less than 10% there are not many active Cu sites on the Co_3O_4

surface, we conclude that Cu doping has a smaller positive effect on the OER activity compared to the dopants Fe, Ni, and V.

Finally, we recognize the strong promoting effect of Cr on the OER activity of Co_3O_4, which is qualitatively comparable to previous experimental studies in the literature.[33–36] Notably, all four $\Delta G_{max}(U)$ values are smaller than zero, indicating that Cr acts as a promoter of OER activity at the auxiliary site, at the active site, and at higher dopant concentrations in the 2TM state. This finding suggests enrichment of the Co_3O_4 surface with Cr sites to enhance OER activity. Our theoretical prediction is experimentally verified below (cf. section 3.6).

3.3 Scaling Relations and Volcano Plot for Doped Co_3O_4(001) Systems

OER activity is inherently limited due to scaling relations, and the main reason for the low activity of electrocatalysts under anodic polarization was attributed to the scaling relationship ΔG_{*OOH} vs ΔG_{*OH} in previous work.[5] This well-accepted paradigm was challenged in a recent contribution by Sokolov and Exner[7], pointing out that the OER volcano plot is more sensitive to the scaling relationship ΔG_{*O} vs ΔG_{*OH} than to ΔG_{*OOH} vs ΔG_{*OH}. For this purpose, it is imperative to investigate the scaling relationships between all OER adsorbates (that is, *OH, *O, and *OOH) and use these scaling correlations to derive potential-dependent volcano plots to comprehend trends in OER activity.

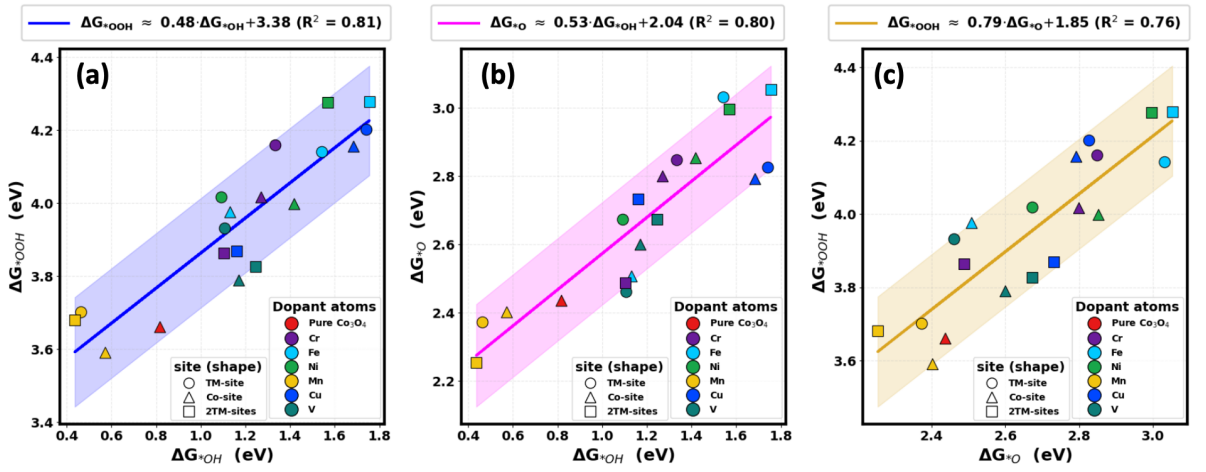

Figure 4. Linear scaling relationships between the OER intermediates (*OH, *O, and *OOH) for pristine and TM-doped Co_3O_4. (a) ΔG_{*OH} vs ΔG_{*OOH}, (b) ΔG_{*O} vs ΔG_{*OH} and (c). ΔG_{*OOH} vs ΔG_{*O}. Each data point corresponds to a specific dopant atom (Fe, Ni, Cr, Mn, Cu, V, or undoped Co_3O_4) and an active site type (TM, Co, and 2TM sites; cf. **Figure 1c**). The fitted regression lines are shown with confidence intervals (shaded regions), along with the slope, intercept, and coefficient of determination (R^2).

Figure 4 shows linear scaling relationships between the adsorption free energies of *OH, *O, and *OOH on Co_3O_4 across the different dopants and site roles (TM, Co, 2TM). Although a

certain degree of scatter can be observed in all three plots, they are still sufficiently linear based on the evaluation of the coefficient of determination. The scaling relationships in **Figure 4** are then used to construct a potential-dependent OER volcano diagram, the details of which are discussed in section S4 of the SI.

Figure 5 shows a mechanistically resolved OER volcano plot at U = 1.37 V vs RHE as a function of the descriptor $\Delta G_{*O} - \Delta G_{*OH}$, while the solid line ("volcano line") corresponds to the minimum free-energy span (envelope $G_{max}^{env}(U = 1.37)$) across the seven reaction mechanisms, which is defined pointwise as

$$G_{max}^{env}(U,\ \Delta G_2) = \min_{m}\ G_{max}^{(m)}(U,\ \Delta G_2) \tag{3}$$

In equation (3), m refers to the respective mechanistic pathway, and $\Delta G_2 = \Delta G_{*O} - \Delta G_{*OH}$. Further details on the construction of the $G_{max}^{env}(U = 1.37)$ envelope is provided in **Figure S2** (cf. section S2.4 of the SI).

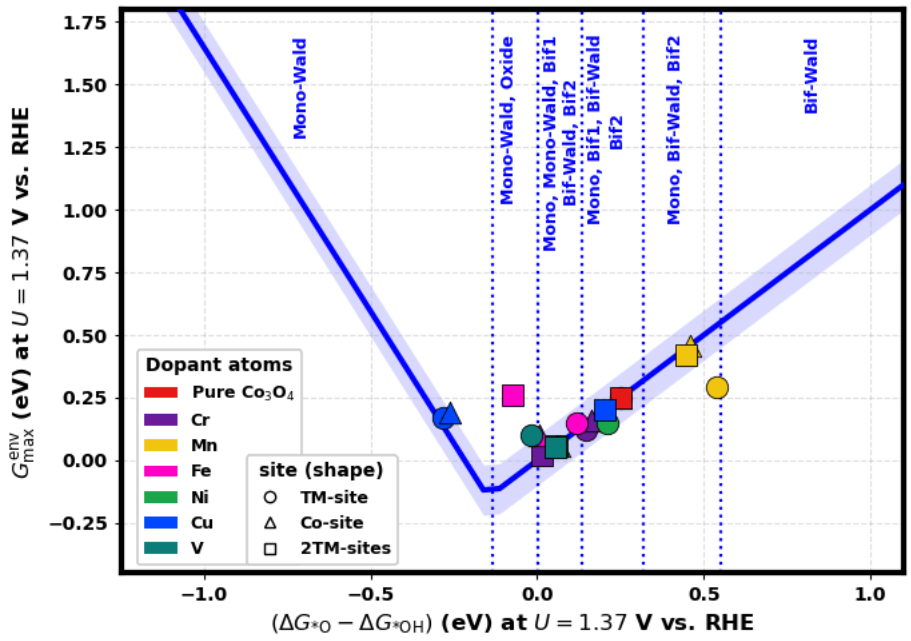

Figure 5. Volcano plot for the oxygen evolution reaction on doped Co_3O_4(001) models with additional information on the preferred reaction mechanism (marked in blue) as derived from the scaling relationships ΔG_{*OOH} vs ΔG_{*OH} and ΔG_{*O} vs ΔG_{*OH} at an applied electrode potential of U = 1.37 V vs RHE. The solid line with shaded bands represents the predicted activity trends based on the scaling relationships, and the shaded area indicates uncertainty of the trend line based on the error bars of the scaling relationships. The vertical dashed lines mark transitions in the energetically favored reaction mechanism, and the preferred mechanistic description is given in each $\Delta G_{*O} - \Delta G_{*OH}$ regime. Note that the symbols correspond to the DFT data (cf. **Figure 2**) for the different dopants (Cr, Fe, Ni, Mn, Cu, V, and undoped Co_3O_4) at different active sites (cf. **Figure 1c**).

It is important to note that **Figure 5** quantifies the uncertainty in the mechanistically resolved volcano plot by adding a narrow sensitivity band around the volcano trend line. This band

results from the error bars of the scaling relationships in **Figure 4**. It is remarkable that of the 19 different configurations (three per dopant and undoped Co_3O_4), 17 fall within the band, and only two outliers (2TM-site of Fe doping and TM-site of Mn doping) are observed. This finding supports the suitability of our methodology to categorize electrocatalysts into active or inactive materials compared to a reference structure (i. e., undoped Co_3O_4) using an advanced volcano approach.

Figure 5 allows quantifying trends in OER activity for the different dopants: while Cr, Fe, Ni, Cu, and V improve the OER activity compared to undoped Co_3O_4 due to a smaller $G_{max}(U)$ value of the doped systems, which is supported by data points closer to the volcano apex, Mn deteriorates the OER performance. These trends are consistent with the analysis presented in **Figure S9** in section S3 of the SI.

Finally, we comment on the progress of our method compared to conventional volcano analyses. The traditional OER volcano plot is derived based on the scaling relationship ΔG_{*OOH} vs $\Delta G_{*OH,}$ assuming a slope of unity and an offset of 3.20 eV, whereas the scaling relationship ΔG_{*O} vs ΔG_{*OH} is omitted from the analysis.[5] Activity predictions are rendered by applying the thermodynamic overpotential, η_{TD}, instead of the span model of $G_{max}(U)$, although the η_{TD} descriptor does not allow for potential-dependent activity analyses. Only the mononuclear mechanism on a single active site is evaluated, while other pathways are ignored. **Figure S11** in section S4 of the SI shows that the conventional volcano approach captures some of the activity trends observed in the volcano plot of **Figure 5**, such as the high activity of Cr-doped Co_3O_4. On the other hand, it should be noted that almost 40% of the data points are not within the sensitivity band around the volcano trend line. In addition, several data points in the volcano in **Figure S11** are located above the volcano apex. This observation is usually attributed to a broken scaling ΔG_{*OOH} vs ΔG_{*OH} and thus to an improved OER performance.[59]

We attribute the differences between the conventional volcano approach and the mechanistically resolved volcano diagram in **Figure 5** to the omission of potential effects (assessment of activity trends under equilibrium conditions rather than OER conditions), the lack of mechanistic diversity (only use of the mononuclear mechanism), and a single active site in the traditional framework. Indeed, observing data points above the volcano apex and interpreting a broken scaling is erroneous, since our analysis (cf. **Figure 4**) reveals that the scaling relationship ΔG_{*OOH} vs ΔG_{*OH} remains intact despite the introduction of dopants. **Figure 5** clarifies that none of the doped Co_3O_4 models reveal activity above the volcano limit

given by the $G_{\max}^{env}$ envelope, and multiple mechanisms govern the OER volcano apex,[58] a situation not observed in the traditional approach (cf. **Figure S11**). Therefore, we conclude that mechanistically resolved trend studies under applied bias are needed to advance catalyst development in OER and avoid false claims of broken scaling relationships. The approach presented in this work can be extended to other OER material classes or electrocatalytic reactions of interest.

3.4 Comparison with Bulk-Doped Co_3O_4

Several experimental works in the literature have investigated doping effects in the OER over Co_3O_4.[27,28,42–46] It is often challenging to map these investigations to theoretically calculated volcano plots based on DFT, since most experimental studies are based on polycrystalline samples rather than single-crystal electrodes. Among the various works, we highlight the contribution by Wei et al[24] who showed, based on a combination of experiment and theory, that V doping enhances OER activity of Co_3O_4. This finding can be explained by the auxiliary site function of the V dopant on the (001) facet of Co_3O_4 (cf. **Figure 3**).

A different situation is encountered with the nanoparticle series reported in a recent work by Schulz and co-workers.[27] There, the authors examined $M_xCo_{3-x}O_4$ with M = Al, V, Cr, Mn, Fe, and Ni at comparable size and morphology with dopant concentrations of 1.6 at%, 3.3 at%, and 6.7 at%. Given that this series of nanoparticles might expose the (001) facet of Co_3O_4 to the same extent per material and the dopant concentration is in the same order of magnitude as in our theoretical framework, a qualitative comparison of our theoretical results with the experimental data of Schulz and co-workers is useful.[27,29,37] The authors observed increased OER activity for V, Cr, Fe, and Ni as dopants, while OER activity decreased for Mn. Note that Cu as a dopant wasn't investigated in this series, whereas Al as a dopant showed reduced OER activity. Among the dopants with a positive catalytic effect on OER activity, the activity trends for these spherical particles at a dopant concentration of 3.3% are V ≥ Cr > Fe > Ni.

We find that the qualitative activity trends of the V, Cr, Fe, Ni, and Mn dopants on the OER activity of Co_3O_4, based on the experimental data[27] are consistent with our theoretical prediction. On the other hand, the volcano plot of **Figure 5** (or **Figure S9** in section S3 of the SI) predicts a quantitative ranking of Cr > V > Ni > Fe. This illustrates that the quantitative trend in OER activity is not entirely reproduced by DFT calculations. We relate these minor deviations to the finding that the nanoparticle series of Schulz and co-workers is based on bulk doping, whereas our atomic-scale models rely on surface doping (cf. **Figure 1c**). To further

quantify the predictive nature of our theoretical model, we compare the trends of OER activity with surface-doped Co_3O_4 samples subjected to pulsed laser treatment (cf. section 3.5) and quantify the promoting effect of Cr doping by synthesizing surface-enriched Cr-Co_3O_4 (cf. section 3.6).

3.5 Comparison with Pulse-Optimized Samples of Surface-Doped Co_3O_4

Surface-doped Co_3O_4 nanoparticles were prepared via pulsed laser defect engineering in liquids (PUDEL; further details are available in section S6 of the SI).[60] V, Cr, Ni, and Fe were introduced from aqueous metal-salt precursor solutions by applying defined numbers of laser pulses to the Co_3O_4 catalyst dispersion in liquid flow. Increasing the pulse number promoted deeper incorporation of dopants into the subsurface, reaching penetration depths of approximately 1.25 nm and 1.50 nm for two and three pulses per volume, respectively.[30] Dopant concentrations were optimized individually to maximize the promotional effect per element. X-ray fluorescence (XRF) analysis revealed higher cation incorporation for iron (3.7 %) and vanadium (2.77 %) compared to chromium (0.16 %) and nickel (below detection limit), likely reflecting differences in incorporation kinetics as well as steric or valence effects.

All doped samples exhibited improved electrocatalytic performance in the OER compared to undoped Co_3O_4, confirming the positive effect of these transition metals on OER activity. In rotating disk electrode measurements at 1.70 V vs RHE for drop-casted catalysts, the activity trend was V > Fe > Cr > Ni, which is possibly linked to variable ion incorporation into the spinel lattice (cf. **Figure 6a-b**). Small additions of Ni and Cr led to at most modest changes, which remain within experimental uncertainty at higher electrode potentials. For catalysts with higher dopant contents, deviations from the undoped baseline become apparent at 1.60 V vs RHE. We note that the activity trend of the laser-treated surface-doped Co_3O_4 nanoparticles differs from the bulk-doped Co_3O_4 samples discussed in section 3.4. This result is relevant for comparing theoretical studies on dopant effects with experimentally tested materials, since a thorough investigation of bulk-doped materials is beyond the scope of conventional DFT models due to the limitation to a few hundred atoms; rather, surface-doped electrocatalysts can be described reasonably well by theoretical models such as the one used in this study (cf. **Figure 1**).

Given that PUDEL enables controlled surface doping to depths of about 1.50 nm, we compare the surface-doped Co_3O_4 nanoparticles to our theoretical predictions (cf. **Figure 5**). We find that theory correctly predicts that all dopants lead to improved OER activity, although the

specific ranking cannot be fully reproduced. While differences between experiment and theory may also be due to the obvious size gap in the systems studied (cf. **Figure S13**), it cannot be ruled out that PUDEL leads to penetration of the dopants into deeper layers than the surface. Therefore, we conclude that an unambiguous comparison of experiment and theory should follow different principles, and we propose to quantify the promoting effects of dopants, as discussed in section 3.2, rather than dopant activity trends, which may depend on many different factors.

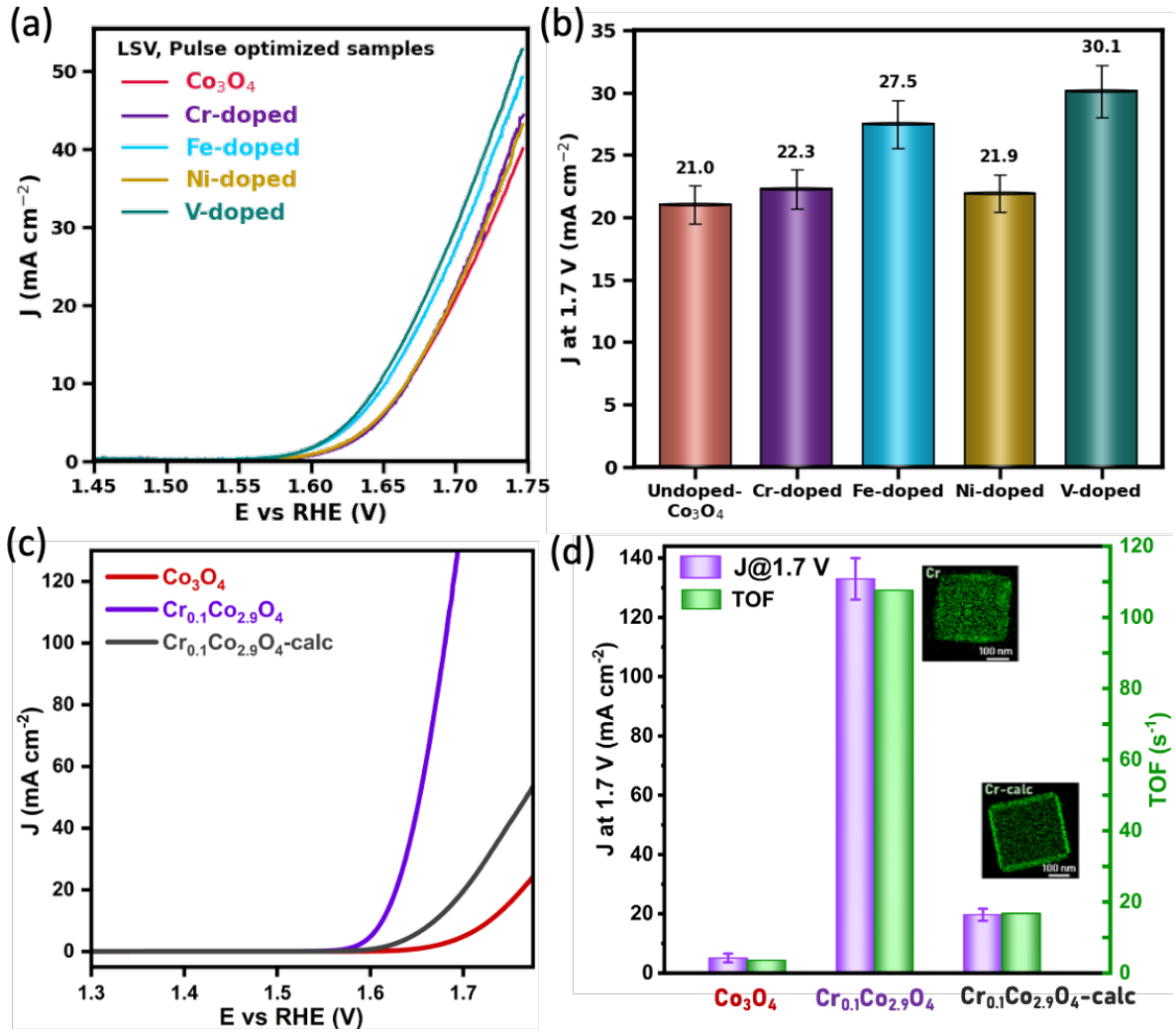

Figure 6. Electrocatalytic OER performance of doped Co_3O_4. (a) Linear sweep voltammograms (LSVs) in the OER potential range scanned with a rate of 5 mV s^{-1}. Dopants were introduced by laser pulse treatment: 3 pulses per volume (PPV) for Cr, Ni, and V, and 2 PPV for Fe. Electrocatalytic measurements were performed in 1 M KOH with a rotating disk electrode (RDE), Pt/C as the counter electrode, and Ag/AgCl (3 M KCl) as the reference electrode. (b) Current density at 1.70 V vs RHE. (c) LSVs (*iR*-compensated) obtained for Co_3O_4, $Cr_{0.1}Co_{2.9}O_4$, and $Cr_{0.1}Co_{2.9}O_4$-calc catalysts in 1.0 M KOH solution at a scan rate of 5 mV s^{-1} and under 1600 rpm rotation of the rotating disc electrode, adapted from our ChemRxiv preprint[37] and (d) Corresponding measured current density for the three electrodes as well as the respective TOF values obtained at 1.7 V vs RHE; Inset shows EDX elemental mapping of Cr-doped samples.

3.6 Experimental verification of the promoted OER activity of Cr-Doped Co_3O_4

Figure 3 indicates that Cr-doped Co_3O_4 reveals the main promoting effect in the OER, particularly if the dopant concentration is increased. This theoretical prediction is verified by synthesizing a Cr-doped, surface-enriched Co_3O_4 nanocube using a hydrothermal method.[37] Details on synthesis and characterization can be found in section S7 of the SI. Particles of well-defined Co_3O_4 and Cr-doped $Cr_{0.1}Co_{2.9}O_4$ nanocubes were microscopically and spectroscopically characterized and showed the same well-defined cubic shape and size (ca. 250 nm edge length), as shown in **Figure S15** (cf. section S7 of the SI). Cr content in the bulk (from EDX) is 4.4% for both pristine and calcinated $Cr_{0.1}Co_{2.9}O_4$, whilst the surface Cr content (from XPS) was 36% and 46% for $Cr_{0.1}Co_{2.9}O_4$ and calcined $Cr_{0.1}Co_{2.9}O_4$, respectively.[37] The linear sweep voltammetry (LSV) curves in **Figure 6c** show that $Cr_{0.1}Co_{2.9}O_4$ exhibits a much higher OER current than undoped Co_3O_4, confirming that the incorporation of Cr into the surface of Co_3O_4 substantially enhances the catalytic performance. After calcination of the pristine $Cr_{0.1}Co_{2.9}O_4$ nanocubes, the $Cr_{0.1}Co_{2.9}O_4$-calc sample maintains its cubic shape and shows Cr enrichment at the nanoparticle surface than in the bulk, as evidenced from TEM-EDX elemental mapping and line-scan analysis (cf. **Figure S16**). Quantitative analysis of the EDX data[37] revealed that the Cr/(Co+Cr) ratio reached up to 40–50% at the cube edges, compared to only 3% in the bulk. This composition mirrors the surface model used for the computations (cf. **Figure 1**), where 50% Cr doping on the Co_3O_4 surface was predicted to increase the OER activity by several orders of magnitude due to a reduction in the ΔG_{max} value (cf. **Figure 3**).

As shown in **Figure 6d**, the current density at 1.70 V vs RHE increased by about five and 25 times for $Cr_{0.1}Co_{2.9}O_4$ and $Cr_{0.1}Co_{2.9}O_4$-calc compared to undoped Co_3O_4, respectively. The corresponding turnover frequency (TOF) values, calculated assuming that only surface Co atoms on the five cube facets are active,[37] also follow this trend: Cr-doped samples exhibit a significantly higher TOF than Co_3O_4. Based on our XPS analysis,[37] the observed enhancement is attributed to Cr-induced modulation of the surface electronic structure, which promotes the formation of more Co^{2+} species readily, which can be easily converted to the active oxyhydroxide phase with octahedral Co^{3+} sites under OER conditions.[61,62] The experimental results demonstrate that surface doping of Co_3O_4 by Cr enhances the intrinsic activity by modulating the surface and electronic structure in a manner favorable for OER, thus confirming the theoretical prediction (cf. **Figure 3**).

4 Conclusion

In the present manuscript, we present a theoretical framework based on electronic structure theory calculations using density functional theory to understand dopant effects in the OER over Co_3O_4. By further developing the concept of volcano plots toward mechanistically resolved volcano diagrams that consider multiple scaling relationships, multiple configurations of active sites, and potential-dependent activity quantification (cf. **Figure 5**), we find that the dopants V, Cr, Fe, and Ni improve the OER activity of Co_3O_4, while doping with Mn or Cu leads to a reduction in OER performance or a negligible contribution, respectively. In contrast to previous theoretical works on this topic, we analyze the promoting effects of the different foreign metals and identify Cr as the most promising dopant (cf. **Figure 3**), since Cr efficiently enhances the electrocatalytic activity at the auxiliary site, the active site, and at higher dopant concentrations.

To benchmark our theoretical calculations, we compare the predicted trends of OER activity of the doped Co_3O_4 models with two different series of Co_3O_4 nanoparticles. One of the series is based on the bulk doping of Co_3O_4,[27] while the other considers surface doping followed by laser treatment[60]. We find that our theoretical framework accurately captures the qualitative impact of dopants on OER activity, while the quantitative trends are not fully reproduced. We attribute this finding to the obvious size gap between atomic-scale models and experimental Co_3O_4 catalysts at the nanoscale. We experimentally validate the theoretical prediction of the promoting effect of Cr-doped Co_3O_4 by synthesizing a well-defined surface-enriched, Cr-doped Co_3O_4 nanocube that significantly enhances the OER activity compared to undoped Co_3O_4. Even at far smaller dopant concentrations, surface doping of Cr into Co_3O_4 nanoparticles by laser pulsing yielded measurable enhancement.

The implications of our work are two-fold: first, the reported approach for quantifying activity trends of doped Co_3O_4 models is a transferable framework that can be equally applied to other materials and electrocatalytic processes. In particular, the potential-dependent volcano plot accounts for the uncertainty in the analysis of adsorption free energies and, compared to the conventional approach, avoids the assertion of broken scaling relationships, which could lead to erroneous interpretation of the OER performance. Second, we argue that inspecting the promoting effects of dopants is a suitable approach to bridge the size gap between atomic-scale models and experimental catalysts and claim that this may be a better way to unambiguously compare theoretical predictions with experimental data. Our work could therefore pave the way

for next-generation theoretical models aimed at catalyst screening in energy conversion and storage, using uncertainty control in volcano plots and promoting effects as levers for the development of advanced catalytic materials.

Acknowledgments

KD, HA, DS, SB, SS, and KSE acknowledge funding from the CRC/ TRR247: "Heterogeneous Oxidation Catalysis in the Liquid Phase" (Project number 388390466, projects A06, C03, and C05). KSE further acknowledges funding by RESOLV Cluster of Excellence, funded by the Deutsche Forschungsgemeinschaft under Germany's Excellence Strategy - EXC 2033 - 390677874 - RESOLV. DB thanks Prof. Vincenzo Amendola (University of Padova) for the opportunity to join the group of Prof. Barcikowski within an ERASMUS program during his master's studies, as well as for the supervision of his master's thesis, part of the results of which are presented in this publication. The group of Prof. Barcikowski thanks Dr. G. Bendt (Inorganic Chemistry, University of Duisburg-Essen) for preparing the Co_3O_4 nanoparticles used in the laser treatment experiments and Jurij Jacobi (Technical Chemistry I, University of Duisburg-Essen) for supervision of the XRF analysis.

References

[1] K. S. Exner, *Adv. Funct. Mater.* **2020**, *30*, 2005060.

[2] S. Back, K. Tran, Z. W. Ulissi, *ACS Appl. Mater. Interfaces* **2020**, *12*, 38256.

[3] B. C. Yeo, H. Nam, H. Nam, M.-C. Kim, H. W. Lee, S.-C. Kim, S. O. Won, D. Kim, K.-Y. Lee, S. Y. Lee, S. S. Han, *npj Comput. Mater.* **2021**, *7*, 137.

[4] S. Divanis, T. Kutlusoy, I. M. Ingmer Boye, I. C. Man, J. Rossmeisl, *Chem. Sci.* **2020**, *11*, 2943.

[5] I. C. Man, H. Su, F. Calle-Vallejo, H. A. Hansen, J. I. Martínez, N. G. Inoglu, J. Kitchin, T. F. Jaramillo, J. K. Nørskov, J. Rossmeisl, *ChemCatChem* **2011**, *3*, 1159.

[6] H. Ooka, J. Huang, K. S. Exner, *Front. Energy Res.* **2021**, *9*, 657336.

[7] M. Sokolov, K. S. Exner, *Chem. Catal.* **2024**, *4*, 101039.

[8] K. S. Exner, *Acc. Chem. Res.* **2024**, *57*, 1336.

[9] M. T. M. Koper, *Chem. Sci.* **2013**, *4*, 2710.

[10] J. Rossmeisl, Z. W. Qu, H. Zhu, G. J. Kroes, J. K. Nørskov, *J. Electroanal. Chem.* **2007**,

607, 83.

[11] Y. Chen, J. K. Seo, Y. Sun, T. A. Wynn, M. Olguin, M. Zhang, J. Wang, S. Xi, Y. Du, K. Yuan, W. Chen, A. C. Fisher, M. Wang, Z. Feng, J. Gracia, L. Huang, S. Du, H.-J. Gao, Y. S. Meng, Z. J. Xu, *Nat. Commun.* **2022**, *13*, 5510.

[12] Z. Zhang, G. Tan, A. Kumar, H. Liu, X. Yang, W. Gao, L. Bai, H. Chang, Y. Kuang, Y. Li, X. Sun, *Mol. Catal.* **2023**, *535*, 112852.

[13] Q. Jiang, S. Wang, C. Zhang, Z. Sheng, H. Zhang, R. Feng, Y. Ni, X. Tang, Y. Gu, X. Zhou, S. Lee, D. Zhang, F. Song, *Nat. Commun.* **2023**, *14*, 6826.

[14] X. Cao, H. Qin, J. Zhang, X. Chen, L. Jiao, *J. Am. Chem. Soc.* **2024**, *146*, 32049.

[15] L. Bai, S. Lee, X. Hu, *Angew. Chem. Int. Ed.* **2021**, *60*, 3095.

[16] K. Dhaka, K. S. Exner, *J. Catal.* **2025**, *443*, 115970.

[17] S. R. Ede, Z. Luo, *J. Mater. Chem. A* **2021**, *9*, 20131.

[18] Y. Peng, H. Hajiyani, R. Pentcheva, *ACS Catal.* **2021**, *11*, 5601.

[19] P. Bothra, S. K. Pati, *ACS Energy Lett.* **2016**, *1*, 858.

[20] M. G. Ahmed, Y. F. Tay, M. Zhang, S. Y. Chiam, L. H. Wong, *ACS Mater. Lett.* **2024**, *6*, 4756.

[21] A. Behera, D. Seth, M. Agarwal, M. A. Haider, A. J. Bhattacharyya, *ACS Appl. Mater. Interfaces* **2024**, *16*, 17574.

[22] S. Liu, L. Kang, J. Hu, E. Jung, J. Zhang, S. C. Jun, Y. Yamauchi, *ACS Energy Lett.* **2021**, *6*, 3011.

[23] Y. Ma, M. Zha, Y. Dong, L. Li, G. Hu, *Mater. Res. Express* **2019**, *6*, 115033.

[24] R. Wei, X. Bu, W. Gao, R. A. B. Villaos, G. Macam, Z.-Q. Huang, C. Lan, F.-C. Chuang, Y. Qu, J. C. Ho, *ACS Appl. Mater. Interfaces* **2019**, *11*, 33012.

[25] J.-Y. Xie, R.-Y. Fan, J.-Y. Fu, Y.-N. Zhen, M.-X. Li, H.-J. Liu, Y. Ma, F.-L. Wang, Y.-M. Chai, B. Dong, *Int. J. Hydrogen Energy* **2021**, *46*, 19962.

[26] L. Li, Q. Xu, Y. Zhang, J. Li, J. Fang, Y. Dai, X. Cheng, Y. You, X. Li, *J. Alloys Compd.* **2020**, *823*, 153750.

[27] C. Placke-Yan, G. Bendt, S. Salamon, J. Landers, H. Wende, U. Hagemann, S. Schulz, *Mater. Adv.* **2024**, *5*, 3482.

[28] T. Grewe, X. Deng, H. Tüysüz, *Chem. Mater.* **2014**, *26*, 3162.

[29] L. Kampermann, J. Klein, T. Wagner, A. Kotova, C. Placke-Yan, A. Yasar, L. Jacobse, S. Lasagna, C. Leppin, S. Schulz, J. Linnemann, A. Bergmann, B. R. Cuenya, G. Bacher, *ACS Catal.* **2025**, *15*, 18391.

[30] S. Zerebecki, K. Schott, S. Salamon, J. Landers, H. Wende, E. Budiyanto, H. Tüysüz, S.

Barcikowski, S. Reichenberger, *J. Phys. Chem. C* **2022**, *126*, 15144.
[31] K. S. Exner, *ACS Catal.* **2020**, *10*, 12607.
[32] S. Razzaq, K. S. Exner, *ACS Catal.* **2023**, *13*, 1740.
[33] C.-C. Lin, C. C. L. McCrory, *ACS Catal.* **2017**, *7*, 443.
[34] Y. Chen, X. Wang, W. He, C. Yu, X. Dang, Z. Zheng, Y. Zhang, *Mol. Catal.* **2023**, *548*, 113410.
[35] P. Mishra, R. Parihar, Y. Singh, A. S. Chaddha, N. K. Singh, *Mater. Today Sustain.* **2024**, *27*, 100826.
[36] W. Liu, J. Bao, L. Xu, M. Guan, Y. Lei, *J. Power Sources* **2020**, *479*, 229099.
[37] C. Placke-Yan, H. Amin, G. Bendt, U. Hagemann, S. Schulz, *ChemRxiv* **2025**, DOI 10.26434/chemrxiv-2025-06g03.
[38] K. Dhaka, S. Kenmoe, A. Füngerlings, R. Pentcheva, K. Tschulik, K. S. Exner, *ChemCatChem* **2025**, *17(19)*, e00992.
[39] A. Bergmann, E. Martinez-Moreno, D. Teschner, P. Chernev, M. Gliech, J. F. de Araújo, T. Reier, H. Dau, P. Strasser, *Nat. Commun.* **2015**, *6*, 8625.
[40] G.-Y. Chen, S.-L. Zhu, X.-Q. Han, D.-C. Wang, J.-C. Zhang, X.-D. Huai, X. Li, F.-Y. Zhang, Z. Xiang, W.-Z. Zhang, *Energy Fuels* **2023**, *37*, 8523.
[41] E. M. Davis, A. Bergmann, H. Kuhlenbeck, B. Roldan Cuenya, *J. Am. Chem. Soc.* **2024**, *146*, 13770.
[42] D. Gorylewski, F. Zasada, G. Słowik, M. Lofek, G. Grzybek, K. Tyszczuk-Rotko, A. Kotarba, P. Stelmachowski, *ACS Catal.* **2025**, *15*, 4746.
[43] M. Yu, C. K. Chan, H. Tüysüz, *ChemSusChem* **2018**, *11*, 605.
[44] X. Deng, C. K. Chan, H. Tüysüz, *ACS Appl. Mater. Interfaces* **2016**, *8*, 32488.
[45] M. Yu, G. Moon, E. Bill, H. Tüysüz, *ACS Appl. Energy Mater.* **2019**, *2*, 1199.
[46] T. Grewe, X. Deng, C. Weidenthaler, F. Schüth, H. Tüysüz, *Chem. Mater.* **2013**, *25*, 4926.
[47] J. P. Fandré, E. Budiyanto, A. Kumar, H. Tüysüz, *ChemCatChem* **2025**, in press.
[48] N. Govindarajan, G. Kastlunger, H. H. Heenen, K. Chan, *Chem. Sci.* **2022**, *13*, 14.
[49] T. Tchakoua, N. Gerrits, E. W. F. Smeets, G.-J. Kroes, *J. Chem. Theory Comput.* **2023**, *19*, 245.
[50] M. Usama, S. Razzaq, C. Hättig, S. N. Steinmann, K. S. Exner, *Nat. Commun.* **2025**, *16*, 6137.
[51] J. K. Nørskov, J. Rossmeisl, A. Logadottir, L. Lindqvist, J. R. Kitchin, T. Bligaard, H. Jónsson, *J. Phys. Chem. B* **2004**, *108*, 17886.

[52] K. Mathew, R. Sundararaman, K. Letchworth-Weaver, T. A. Arias, R. G. Hennig, *J. Chem. Phys.* **2014**, *140*, 084106.

[53] R. Urrego-Ortiz, S. Builes, F. Illas, F. Calle-Vallejo, *EES Catal.* **2024**, *2*, 157.

[54] L. P. Granda-Marulanda, A. Rendón-Calle, S. Builes, F. Illas, M. T. M. Koper, F. Calle-Vallejo, *ACS Catal.* **2020**, *10*, 6900.

[55] J. Cheng, P. Hu, P. Ellis, S. French, G. Kelly, C. M. Lok, *J. Phys. Chem. C* **2008**, *112*, 1308.

[56] M. J. Craig, G. Coulter, E. Dolan, J. Soriano-López, E. Mates-Torres, W. Schmitt, M. García-Melchor, *Nat. Commun.* **2019**, *10*, 4993.

[57] H. Chen, L. Shi, X. Liang, L. Wang, T. Asefa, X. Zou, *Angew. Chem. Int. Ed.* **2020**, *59*, 19654.

[58] K. S. Exner, *Mater. Horiz.* **2023**, *10*, 2086.

[59] N. B. Halck, V. Petrykin, P. Krtil, J. Rossmeisl, *Phys. Chem. Chem. Phys.* **2014**, *16*, 13682.

[60] K. Lau, S. Zerebecki, L. Pielsticker, W. Hetaba, K. Dhaka, K. S. Exner, S. Reichenberger, S. Barcikowski, *Adv. Mater. Interfaces* **2024**, *11*, 2302396.

[61] H. M. A. Amin, C. J. Bondue, S. Eswara, U. Kaiser, H. Baltruschat, *Electrocatalysis* **2017**, *8*, 540.

[62] Z. Liu, H. M. A. Amin, Y. Peng, M. Corva, R. Pentcheva, K. Tschulik, *Adv. Funct. Mater.* **2023**, *33*, 2300847.

TOC Graphic

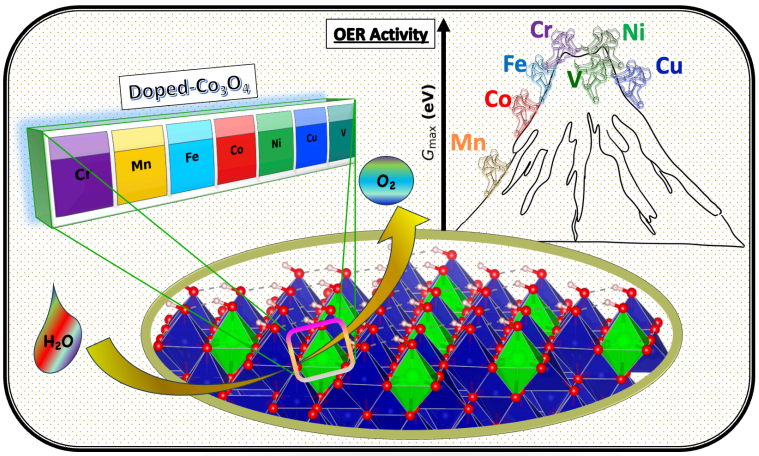

Twitter

Personal:

@ExnerKai

Institute:

@unidue

@cenide_unidue

@SolvationSci